

Deep Learning Analysis of Polaritonic Wave Images

Suheng Xu, Alexander. S. McLeod, Xinzong Chen, Daniel J. Rizzo, Bjarke S. Jessen, Ziheng Yao, Zhicai Wang, Zhiyuan Sun, Sara Shabani, Abhay N. Pasupathy, Andrew J. Millis, Cory R. Dean, James C. Hone, Mengkun Liu, and D. N. Basov*



Cite This: ACS Nano 2021, 15, 18182–18191



Read Online

ACCESS |

Metrics & More

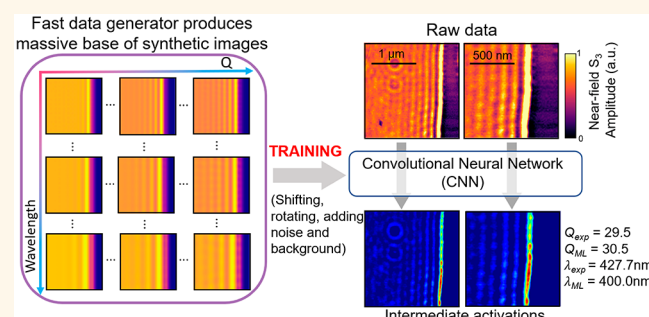
Article Recommendations

Supporting Information

ABSTRACT: Deep learning (DL) is an emerging analysis tool across the sciences and engineering. Encouraged by the successes of DL in revealing quantitative trends in massive imaging data, we applied this approach to nanoscale deeply subdiffractive images of propagating polaritonic waves in complex materials. Utilizing the convolutional neural network (CNN), we developed a practical protocol for the rapid regression of images that quantifies the wavelength and the quality factor of polaritonic waves. Using simulated near-field images as training data, the CNN can be made to simultaneously extract polaritonic characteristics and material parameters in a time scale that is at least 3 orders of magnitude faster than common fitting/processing procedures. The CNN-based analysis was validated by examining the experimental near-field images of charge-transfer plasmon polaritons at graphene/ α -RuCl₃ interfaces. Our work provides a general framework for extracting quantitative information from images generated with a variety of scanning probe methods.

KEYWORDS: s-SNOM, polariton, vdW materials, deep learning, convolutional neural network

Polaritons, hybrid collective modes of light and polar resonances in materials, are of high interest in the fields of nanophotonics and quantum information processing.^{1–4} Various types of polaritons have been observed in van der Waals materials, where photons couple to plasmons, phonons, excitons, or Cooper pairs and form robust hybrid modes.^{5–14} The wavelengths λ_p of polaritons are reduced compared to the wavelengths λ_0 of free space photons by orders of magnitude.¹ It is therefore said that polaritons are highly confined on subwavelength length scales. The reason behind the immense utility of polaritons is that the response function of a material can be inferred from the visualization of the polaritonic interference patterns.^{7,13,15–17} A common way to launch and image polaritons is based on the scattering-type scanning near-field optical microscope (s-SNOM).^{4,18} Here, the tip of an atomic force microscope (AFM) scatters the free propagating light into evanescent waves with high in-plane momentum on the order of the inverse of the tip radius; this simultaneously excites the polaritons and outcouples the confined near field into the far field (shown schematically in Figure 1(a)). Raster scanning the illuminated AFM tip near a material surface thus generates a map of the local near-field signal with a high spatial resolution (~10 nm). Here, polaritons present as periodic fringes in the near-field



amplitudes. These images can be used to reconstruct the energy-momentum dispersion by fitting the frequency-dependent spatial line profiles with a functional ansatz.^{7,16,17} However, this fitting procedure is time-consuming and is difficult to automate. The predicament stems from the complex interferences of polaritons, especially when a small sample size, in combination with low damping, permits multiple cavity-like reflections by polaritonic waves.^{5,6,11,15,19–21} In this work, we have developed a deep learning (DL) routine for the fast extraction of crucial polaritonic parameters from nano-IR images with little human assistance. Furthermore, we document the utility of this approach by analyzing polaritonic fringes at the interface of two atomically layered van der Waals materials: graphene and α -RuCl₃.

Deep learning is a branch of artificial intelligence that is commonly employed for rapid quantitative analysis across

Received: August 13, 2021

Accepted: October 26, 2021

Published: October 29, 2021



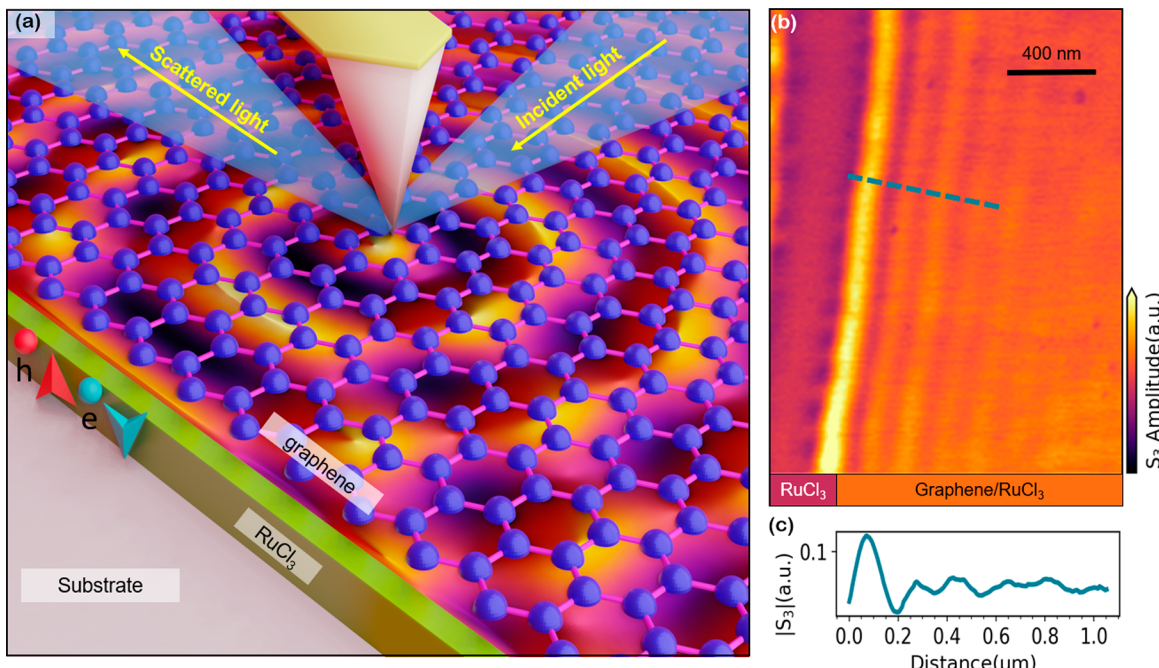


Figure 1. Scanning polariton interferometry of an hBN/Graphene/α-RuCl₃/SiO₂ heterostructure. (a) Schematics of surface polaritons excited by focused continuous wave (CW) light, impinging on an AFM tip. The local near-field response under the tip is obtained by collecting the scattered field in the far field. (b) Map of the near-field amplitude on an hBN/graphene/α-RuCl₃/SiO₂ heterostructure ($T = 80$ K, $\omega = 898$ cm⁻¹). The profile of the oscillating fringes in the bulk indicates the presence of surface plasmon polaritons. (c) Line profile of surface plasmon polaritons along the dashed line in (b).

disciplines.^{22–24} Starting in the 1990s with experimental particle physics, DL has impacted many subfields of physics.^{25–30} Notably, DL algorithms reveal data trends with minimal assumptions.³¹ DL-enabled advances in scanning probe microscopy include the ability to identify translational-symmetry-breaking states,³² quantitative analysis of the optical signal in s-SNOM experiments,^{33,34} accelerated analysis of raster-scanned images,³⁵ and automated scanning probe microscopy without user control.³⁶ Here, we analyze the polariton images with a convolutional neural network (CNN) that is commonly used for image classification.^{37,38} We demonstrate that the CNN can capture key features in nano-IR images produced by polariton interference patterns. The CNN trained with only synthetic data was nevertheless capable of accurately extracting wavelengths and quality factors from the experimental nano-IR images. We focus on the analysis of surface plasmon polaritons (SPPs) in graphene/α-RuCl₃ as a case study.²¹ We also demonstrate that the CNN is capable of dealing with more complex polaritonic interference patterns that are formed by the superpositions of modes with different wavelengths. Our results indicate that DL-based analysis of polariton images offers an efficient high-fidelity alternative to traditional data processing methods, providing the conceptual bedrock for similar future applications.

SCANNING POLARITON INTERFEROMETRY

In this section, we provide a primer on nanoinfrared visualization of polaritonic waves. Figure 1(a) depicts the working principle of scanning polariton interferometry based on s-SNOM. The tip-launched surface polaritons (SPs) can be reflected by edges of the sample, defects, grain boundaries, and other forms of structural/electronic inhomogeneities.¹⁹ The reflected SPs interfere with the outgoing SP wave, forming a

standing wave pattern. Since the far-field signal is determined by the local electric field strength under the AFM tip, raster scanning the tip leads to a spatial interferogram. Both the amplitude and the phase of the tip-scattered signal can be obtained in the pseudoheterodyne detection scheme.^{18,39} In s-SNOM, the AFM tip oscillates at the mechanical resonance frequency Ω , and the background signal can be highly suppressed by demodulating the scattered signal to higher harmonic orders of the tapping frequency ($n\Omega$, $n \geq 2$). In Figure 1(b), we present the near-field amplitude images obtained for an hBN/graphene/α-RuCl₃/SiO₂ heterostructure near the graphene edge. Here, the periodic fringe pattern emanating perpendicular to the edge corresponds to distinct types of polaritonic waves: tip-launched SPs and also edge-launched SPs.²¹ The edge-launched polaritons produce oscillations of the wavelength λ_p , and the tip-launched polaritons complete round trips between the cantilever and the sample edge, leading to oscillations at $\lambda_p/2$.¹⁷

The propagating nature of polaritons can be characterized by a complex wavevector $q_p = q_1 + iq_2$, which depends on the effective dielectric function of the environment, in-plane conductivity, and frequency.^{1,6} The wavelength of the polaritons is determined by the real part of the wavevector as $\lambda_p = \frac{2\pi}{q_1}$ and the quality factor is defined by the ratio $Q = \frac{q_1}{q_2}$ between the real part and the imaginary part of the wavevector. Since s-SNOM visualizes the standing wave pattern of polaritons, the distance between two fringes is half of λ_p for tip-launched round-trip polaritons. By evaluating the wavelength and quality factor from near-field intensity profiles, the local electronic properties (e.g., Fermi level and scattering rate) can be obtained.^{6,11}

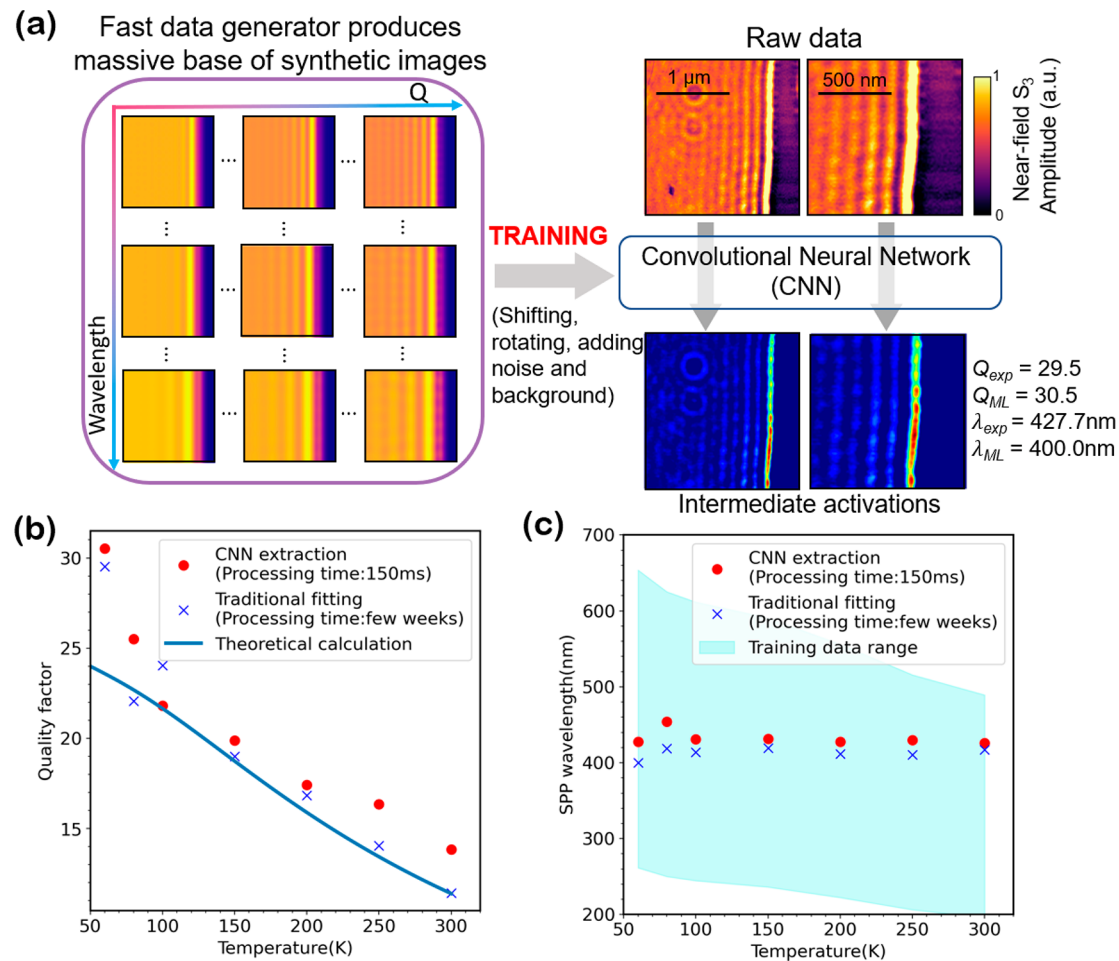


Figure 2. Training, application, and extraction results of CNN-based analysis of polaritonic images. (a) Workflow of CNN training and applications. A numerical solver package is used to generate a massive set of polaritonic images labeled with different combinations of wavelengths and quality factors. After adding noise to the synthetic images, the data are fed into the CNN for training. The trained CNN then extracts both the quality factor and the wavelength from the input experimental data. The intermediate activation visualization shows that the CNN captures key features of the polaritonic patterns. (b) Quality factor plotted versus sample temperature evaluated by conventional manual fitting (blue crosses) and CNN extraction (red dots). The solid line is the theoretical model introduced from ref 21. (c) Polaritonic wavelength plotted versus temperature evaluated by common fitting (blue crosses) and CNN extraction (red dots).

RESULTS AND DISCUSSION

Deep Learning Analysis of Charge-Transfer Plasmon Polaritons. Here, we introduce a CNN-empowered method for analyzing polaritonic images. Fed with 1725 synthetic near-field images generated by numerical simulations, a trained network was capable of extracting both the quality factor and the wavelength from an experimental near-field image within 150 ms. In Figure 2(a), we show the workflow for training and applying the CNN for polaritonic image analysis. To generate synthetic near-field images as training data, we employed a recently reported simulation model, which successfully reproduced the near-field signal of surface plasmon polaritons reflected at a point defect.²¹ In the simulation, the near-field antenna probe was approximated as a point dipole. The scattering signal was evaluated by the generalized reflection coefficient of the probe with spatial dependence. The area for simulation was limited to $4 \times 4 \mu\text{m}^2$ with a spatial resolution of 10 nm. A square plasmonic medium was located at the center of the substrate, and the near-field intensity was recorded near the boundary of the sample. All simulated near-field signals were normalized into a range of 0 to 1 to simplify the network training. Synthetic near-field images were labeled with

wavelengths λ_p varying from 73 to 167 nm and quality factors Q ranging from 5 to 30. An additional background signal and noise were added to the simulated near-field signal to mimic experimental data (see Supporting Information). To endow the CNN with the ability to make accurate extractions regardless of the orientation of sample boundaries in the images, we applied data augmentation to the training data set. By randomly shifting and rotating the images, we generated sets of near-field images much more similar to experimental results and consequently enhanced the generalization of the CNN (see Supporting Information). A validation data set generated with randomly distributed parameters acted as a metric to evaluate the generalization error of the CNN.

As a proof-of-principle demonstration, we applied the trained CNN to the temperature-dependent data for charge-transfer plasmon polaritons for $\alpha\text{-RuCl}_3/\text{graphene}$ interfaces.²¹ Due to the large work function difference between $\alpha\text{-RuCl}_3$ and graphene (6.1 versus 4.6 eV, respectively), charge carriers in excess of 10^{13} cm^{-2} are transferred across the 2D interface between the two constituent materials. The net effect of the charge transfer is that the Fermi energy in graphene is subsequently shifted by 0.6 eV with respect to the charge

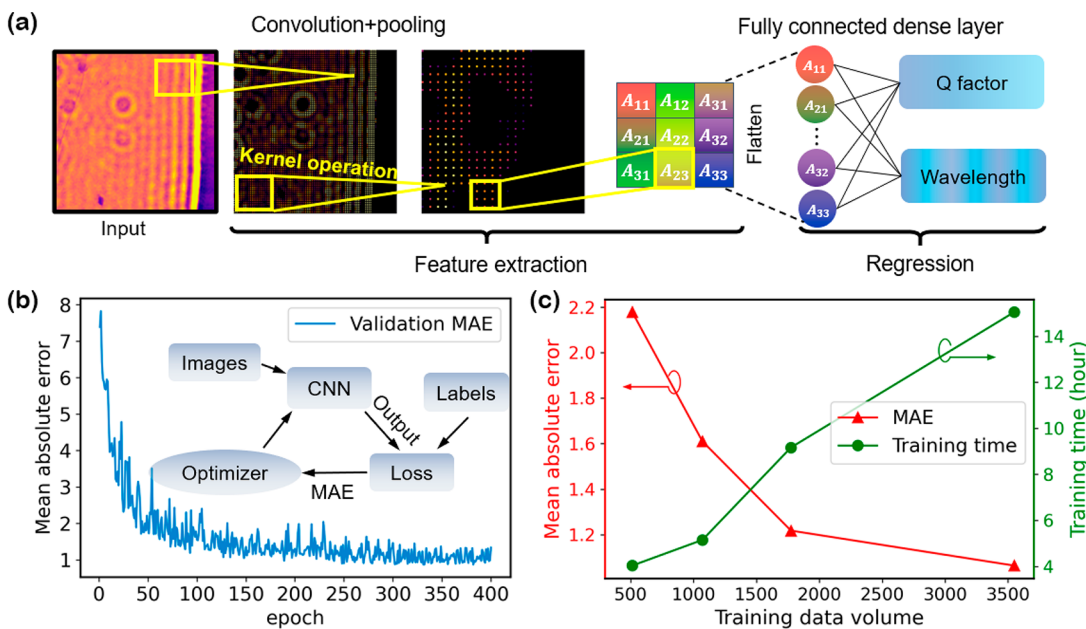


Figure 3. (a) Schematics of CNN architecture for polaritonic near-field image analysis. The CNN is composed of two blocks intended for feature extraction and numerical regression. The convolution and max-pooling operations extract and abstract the local patterns in the image. Then, the output tensor is flattened into an array, which becomes the input for the following fully connected dense layer for regression. The outputs of the CNN are the quality factor and the wavelength of the polariton in the near-field image. Here, the convolution operations are visualized by the intermediate activation visualizations (see [Supporting Information](#)). (b) The mean absolute error as a function of epoch in the training process. Inset: A simplified version of the flowchart for the network training. (c) The mean absolute error and training time as functions of training data volume.

neutrality point. Thus, the undoped graphene becomes highly metallic without resorting to chemical doping or back gating, as indicated by the distinct polaritonic interference patterns observed by s-SNOM ([Figure 1\(b\)](#)). Furthermore, this massive charge transfer may also lead to the emergence of the topological quantum spin liquid state in α -RuCl₃.^{40,41} Here, we selected square regions in the experimental nano-IR images that included the graphene boundary and the polaritonic fringe patterns (see [Supporting Information](#)). We analyzed relatively large regions containing evident interference fringes in order to enhance extraction accuracy. This procedure assures better fidelity of parameter extraction compared with the fitting of individual line scans. In each nano-IR image, the near-field amplitude is normalized into the range of 0 to 1 before extraction. Since the scales of pixels in the measurement depend on the temperature, the range of the training data set varies at different temperatures. The extracted quality factors and wavelengths shown in [Figure 2\(b\)](#) and (c) agree well with the values obtained from the traditional fitting. The small discrepancy between the parameters generated with the two approaches (<13.5%) might come from a combination of intrinsic uncertainty of the CNN, the difference between simulation data and experimental data, and the inhomogeneous nature of samples. We conclude that the CNN successfully extracted the temperature-dependent quality factors and wavelengths from the raw data with relatively high accuracy. Notably, the entire extraction process took less than 150 ms for 14 different images, highlighting the efficiency of DL analysis compared with the traditional fitting.

Convolutional Neural Network for Polaritonic Near-Field Image Analysis. The superiority of the CNN for polaritonic nano-IR image analysis is rooted in the working principles and the architecture of the CNN.³¹ Previously,

CNN-based architectures have been well suited for complex image recognition tasks and have even outperformed humans in tasks such as facial recognition.⁴² As a subtype of the neural network, the matrix operations in several layers are replaced by convolutional operations. The typical architecture of the CNN is presented in [Figure 3\(a\)](#). An input near-field image first goes through a series of convolution layers and pooling layers, which extract the local features and decrease the effective dimensions of the image. The information in the original data is distilled into more abstract patterns in deeper convolution layers. After going through the last convolution layer, the tensors are flattened and processed onward to fully connected dense layers whose outcomes are the quality factor and the wavelength. Compared with the fully connected dense layers, the convolution and pooling operations in the CNN improve both speed and accuracy. Since the convolution kernel can effectively capture the local patterns and operate several convolution layers simultaneously, the CNN will eventually gain a powerful feature extraction capability for global information. In addition, fewer free parameters are required to train the CNN compared with the fully connected neural network. Though the degrees of freedom of the network are decreased, the network maintains the same performance for extracting polaritonic parameters. Moreover, the CNN identifies patterns in a translationally invariant way, and the extraction results are robust to small translations of the input features.⁴³ Hence, the near-field images do not need to be manually rotated or positioned as part of the parameter extraction procedure.

The details of our CNN architecture are presented in the [Supporting Information](#). The capacity of the network can be altered if the complexity of the training data set increases. We chose the rectified linear unit (ReLU) as the activation

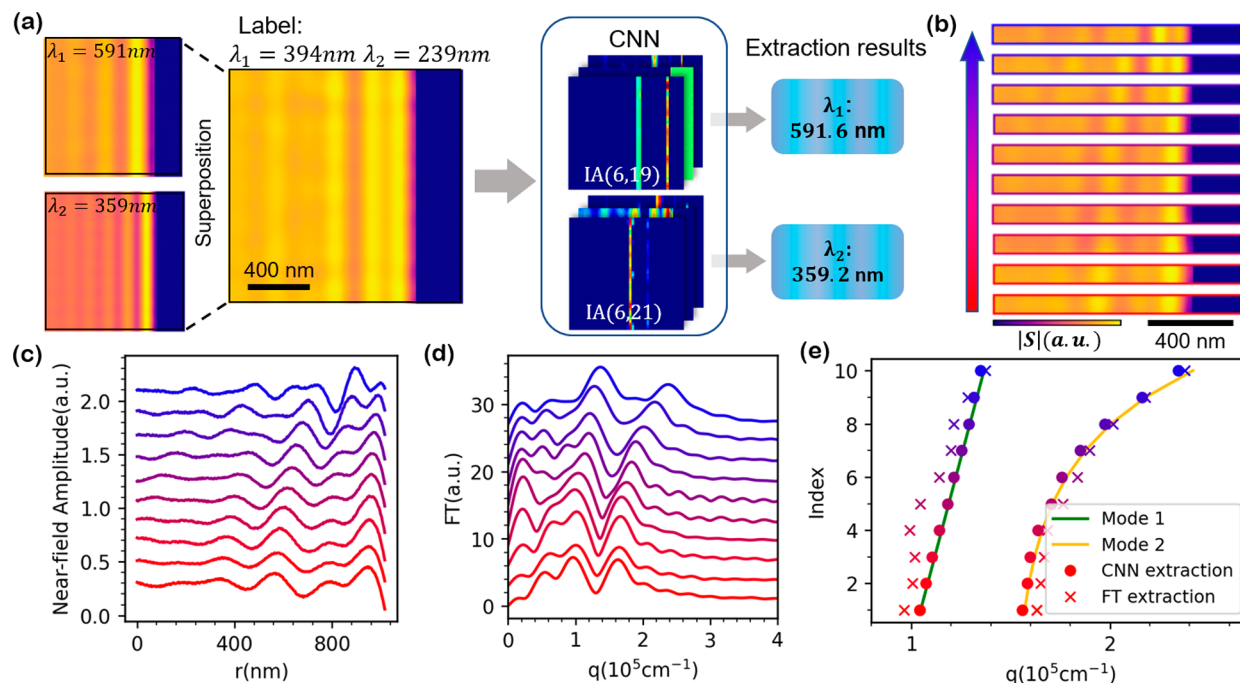


Figure 4. CNN-based multiwavelength parameter extraction. (a) Schematics of workflow required for analysis of nano-IR images. The multiwavelength data were generated via a superposition of the two simulated single-wavelength polaritonic images and were labeled with the two wavelengths. Representative outputs from intermediate activations (IA channels 19 and 21 in layer 6) attest that the CNN extracted the fringes corresponding to individual polariton modes. (b) Synthetic polaritonic images generated by combinations of polaritons at two different wavelengths. (c) Line profiles of the synthetic nano-IR images shown in (b). (d) Fourier transform (FT) of the line profiles in (c). (e) Comparison among the simulation parameters, CNN extraction results, and FT extraction results.

function, which introduced the nonlinearity between the input and output of the network. The loss function was defined as the mean absolute error (MAE) between the extracted values and the labels. The root mean square prop algorithm was applied to optimize the network in the training process.⁴⁴ In each epoch, all the training data were fed into the CNN, and the free parameters in the CNN were tuned to reduce the loss function based on the chosen algorithm. The network training process converged after a sufficient number of epochs, and the signature of the convergences could be visualized by the MAE loss as a function of epochs, as shown in Figure 3(b). The total training time was around 15 h. The network training was boosted based on GPU acceleration (GTX 1050Ti), and the total time for training can be further reduced with the assistance of more powerful computational hardware. To provide a reference for future CNN development, we also studied the relationship among the MAE loss, the training time, and the training data volume. The results are summarized in Figure 3(c). The MAE loss, evaluated by the same set of validation data sets, monotonically decreased when the training data set was larger. The training time was still in a reasonable range of 15 h, and the number of data points was 3500. However, since the validation data set was also generated by the same simulation package, the MAE cannot fully evaluate the accuracy of the CNN in making extractions on realistic data. To unambiguously evaluate the accuracy of a CNN, a validation data set composed of labeled experimental data should be applied in the future.

CNN for Multiwavelength Data Extraction. The CNN-based parameter extraction can be generalized to apply to more complex nanoimaging data. In this section, we show that the CNN is capable of quantifying polaritonic oscillations with

multiple wavelengths that are simultaneously present in the same field of view of nano-IR images. For example, complex profiles of near-field amplitude composed of multiple waveguide modes are commonly observed in hyperbolic vdW materials.^{8,16,45–47} When the thickness of the crystal is relatively large, the air mode and multiple waveguide modes can be simultaneously excited and probed by s-SNOM.^{48,49} However, the analysis toolset suitable for processing the multiwavelength data are limited. Fourier transformation (FT) is widely applied to separate multiple modes in momentum space,^{7,9,49–51} but its accuracy suffers when the polaritonic data are impacted by losses with only a few fringes seen in raw images.

The schematics of the multiple-wavelength extraction based on the CNN are shown in Figure 4(a). We created the multiwavelength training data set by superposing two single-wavelength polariton images. Each composite image was labeled with two wavelengths corresponding to the two individual polariton images. The ranges of labels were evenly distributed from 260 to 400 nm and from 460 to 600 nm for λ_1 and λ_2 , respectively. The quality factor for each polaritonic near-field image was randomly distributed from 10 to 15. The noise and signal on the substrate were generated in a similar manner and are shown in the Supporting Information. The CNN was then trained with 900 near-field images; the MAE went below 5 nm by the end of the training process.

In Figure 4(a), we illustrate the generation and extraction processes for one multiwavelength near-field image. The extracted wavelengths are consistent with the labels of synthetic images. Moreover, we also observe from the intermediate activation visualization that the CNN was able to extract at least two fringes corresponding to each

wavelength in the feature extraction process. To further explore the utility of the CNN for multiwavelength extraction, we generated 10 synthetic near-field images that are shown in Figure 4(b). The parameters for the simulation were selected along the two traces presented in Figure 4(e). These 10 synthetic images purposefully fall outside the training data set. In Figure 4(c), we show that it is hard for the extracted line profiles and the multiple modes corresponding to different wavelengths to be directly recognized by the human eye. The Fourier transform (FT) of the line scan (Figure 4(d)) shows two distinct peaks, and the momenta for different modes can be extracted by recording the positions of peaks on the q axis. The comparison between the FT and the CNN extraction results is summarized in Figure 4(e). The CNN demonstrates an overall consistency, while the FT deviates from the ground state, especially in the low momentum region. Again, the CNN-based extraction for multiwavelength polariton images does not require any image preprocessing and enables direct analysis on raw nano-IR images in the time scale of tens of milliseconds. To sum up, we have documented the accuracy and efficiency of multiwavelength extraction based on the CNN. The preliminary results attest that the CNN is an important candidate for analyzing polaritonic images with high complexity.

CONCLUSIONS

In this study, we have demonstrated that the CNN can efficiently extract the key quantitative parameters from polaritonic nano-IR images, including wavelengths and quality factors. The current CNN trained with synthetic data successfully extracted the temperature-dependent quality factors and wavelengths for the charge-transfer plasmon polariton at the graphene/ α -RuCl₃ interface. Furthermore, we have also shown that the CNN can potentially extract multiple wavelengths that correspond to different waveguide modes simultaneously detected in the same field of view. The CNN-based polaritonic near-field analysis is able to extract the wavelengths and quality factors over tens of milliseconds, which significantly accelerates the overall data processing. This large improvement in terms of parameter extraction is fundamentally important for future scanning polariton interferometry studies, where massive amounts of data are expected to be generated on a routine basis.

The current CNN is trained to work with the interference patterns of polaritons that are scattered by straight sample boundaries. An extension to circular polaritonic patterns caused by point defects is rather trivial. The CNN can also work on polaritonic data collected for more complex device geometries and architectures (e.g., curved edges and polaritonic cavities) once the corresponding training data are utilized in the training process. Furthermore, inactive channels in the convolution layers are well suited to adapting the current CNN to enable the recognition of even more complex interference patterns (see Supporting Information). Moreover, errors in the CNN-based procedure can be reduced by including real data in the training sets, a procedure known as transfer learning.⁵² Existing experimental data can be utilized for further evaluations and optimizations of the network. In addition, sophisticated DL models and algorithms (e.g., Resnet⁵³ and Senet⁵⁴) can be applied to achieve even more ambitious goals by increasing the number of convolution layers and introducing the channels' interactions.

In this work, we limited ourselves to the analysis of nano-IR polariton images, though this CNN-based regression analysis approach is generic to parameter extraction tasks for other nanoprobe measurements. In a recent nanoprobe study, the tomography, local conductivity, and local magnetism can be simultaneously resolved by utilizing multimessenger nanoprobos.⁵⁵ The multimessenger measurements enlarge the dimensionality of the data and, empowered by DL, might lead to more accurate and informative inferences. The nanospectroscopic data also possess copious information about the tomography,^{56,57} phase transitions,^{58,59} and local electronic structures of the materials.^{60,61} Moreover, the DL-based image analysis can be extended to different scanning probe measurements, such as scanning tunneling microscopy, where the quasiparticle interference manifests itself as periodic spatial variations in the local density of states.^{62–64} The DL-based analysis of these high-dimensional nanospectroscopic data is a promising direction for future investigation.

METHODS

Simulation Method. To generate predicted real-space images shown in the main text, we apply a semianalytic method that approximates the near-field scattering signal from a 2D material as proportionate (to first order) by the z -polarization of a polarizable dipole raster scanned (at a height $z = z_{dp}$) some tens of nanometers over the surface of a sample (at $z = 0$):

$$S(\rho_{dp}) \sim p_z \approx \alpha E_{ref,z}(\rho_{dp}, z = z_{dp}) \quad (1)$$

Here α denotes the dipole polarizability, $E_{ref,z}$ denotes the z -component of the electric near field reflected by the sample in response to the incident dipole field; and ρ_{dp} denotes evaluation at the in-plane coordinate of the probe. Although this expression represents only the first term in a Born expansion of the full self-consistent dipole polarization,⁶⁵ a similar conceptual treatment was previously shown to faithfully replicate the polaritonic near-field response of two-dimensional materials as measured by scanning near-field optical microscopy.⁶⁶ Here, we summarize the key points enabling our calculation of eq 1 in the quasi-electrostatic approximation and defer more detailed discussion to forthcoming work.

We recast eq 1 in a form reminiscent of the local photonic density of states⁶⁷ measured at the location $r_{dp} = (\rho_{dp}, z_{dp})$ of our dipole probe:

$$\begin{aligned} S(\rho_{dp}) \sim \int_{z>0} dV \hat{j}_{dp} \vec{E}_{ref} &= \int_{z>0} dV \nabla \cdot \hat{j}_{dp} \Phi_{ref} \\ &\propto \int_{z>0} dV - Q_{dp} \Phi_{ref} \end{aligned} \quad (2)$$

Here \hat{j}_{dp} denotes the unit vector oriented along the direction of the point dipole current; Q_{dp} denotes the instantaneous charge distribution associated with the dipole; and Φ_{ref} is the electrostatic potential for the reflected field given by $\vec{E}_{ref} = -\nabla \Phi_{ref}$. Now $S(\rho_{dp})$ can be evaluated entirely in the plane $z = 0$ by identifying the “incident” electrostatic potential generated by the dipole through $Q_{dp} = -\frac{1}{4\pi} \nabla^2 \Phi_{dp}$ and integrating eq 2 by parts, yielding:

$$\begin{aligned} \int_{z>0} dV - Q_{dp} \cdot \Phi_{ref} &= \frac{1}{4\pi} \left[\int_{z=0^+} dA (-\hat{z} \cdot \nabla \Phi_{dp}) \Phi_{ref} \right. \\ &\quad \left. - \int_{z>0} dV \nabla \Phi_{dp} \cdot \nabla \Phi_{ref} \right] = \frac{1}{4\pi} \int_{z=0^+} dA (\Phi_{dp} \partial_z \Phi_{ref} - \partial_z \Phi_{dp} \Phi_{ref}) \end{aligned} \quad (3)$$

Here, we have applied the source-free condition $\nabla^2 \Phi_{ref} = 0$ in the volume $z > 0$. Equation 3 represents an approximation for the signal $S(\rho_{dp})$ when Φ_{dp} is produced from a dipole-like probe at r_{dp} . Further simplification is admitted by the fact that $\Phi_{ref} = -\hat{R} \Phi_{dp} \equiv -\Phi_R$ with \hat{R} being a generalized reflection operator. Moreover, for scalar potentials, $\Phi_{1,2}$ harmonic (viz. source-free) in the plane of integration,

$\int dA \Phi_1 \partial_z \Phi_2 = \pm \int d^2 q |\mathbf{q}| \tilde{\Phi}_1 \tilde{\Phi}_2$, where tilde quantities represent in-plane Fourier transforms with respect to the momentum \mathbf{q} , and \pm corresponds to the cases where Φ_2 is sourced from $z > 0$ or $z < 0$, respectively. With these considerations, eq 3 reduces to

$$S(\rho_{dp}) \sim \frac{1}{2\pi} \int d^2 q |\mathbf{q}| \tilde{\Phi}_{dp} \tilde{\Phi}_R = \frac{1}{2\pi} \int dA (q^* \Phi_{dp}) \hat{R} \Phi_{dp} \quad (4)$$

where $(q^* \Phi_{dp})$ represents the incident scalar potential spatially convolved at $z = 0^\circ$ with a sharpening function with Fourier kernel $|\mathbf{q}|$. Equation 4 represents a norm of the function Φ_{dp} in the plane $z = 0$ with respect to the composite reflection operator $q^* \hat{R}$.

By way of demonstration, we can consider cases where the reflected field is given by $\tilde{\Phi}_R = r_p(q) \tilde{\Phi}_{dp}(q)$, with r_p being the momentum-resolved Fresnel coefficient for, e.g., a layered medium with in-plane translational invariance. Applying the in-plane Fourier transform of the dipole potential $\tilde{\Phi}_{dp}(\mathbf{q}) = e^{-qz_{dp}}$ at $z = 0$, for such cases eq 4 evaluates to $S \propto \int dq r_p(q) q^2 e^{-2qz_{dp}}$. This is indeed the first-order term in a Born series expansion of the point dipole model widely used to predict near-field observables in the case of multilayered systems.^{68,69} Meanwhile, whereas the real-space counterpart that we present in eq 4 remains underreported, it provides a powerful means to predict images recorded by scanning near-field optical microscopy.

We now briefly describe our method for evaluating $\hat{R} \Phi_{dp}$ in the case of a spatially inhomogeneous 2D material at $z = 0$ described by a (piecewise) optical conductivity $\sigma_{2D}(\rho)$ upon a substrate with isotropic reflectivity β_{subs} . We first consider the integro-differential equation for the scalar potential Φ_{ref} generated by σ_{2D} in response to the potential Φ_{dp} of our quasi-dipolar probe,⁷⁰ in the absence of a substrate:

$$\left[1 + V^* \frac{1}{2\pi q_p} \nabla \cdot \bar{\sigma}(\rho) \nabla \right] \Phi(\rho) = \Phi_{dp}(\rho), \text{ with } \Phi = \Phi_{dp} + \Phi_{ref} \quad (5)$$

Here q_p denotes the complex plasmon wavevector associated with our plasmonic medium, and $\bar{\sigma}(\rho)$ is a piecewise homogeneous function equal to 0 or 1 marking the lateral region $\rho \in \Omega_p$ occupied by the plasmonic domain. Although in the present work we consider only a single domain plasmonic medium, this prescription more generally allows us to generate training data even for multidomain plasmonic structures. Meanwhile, $V(r, r') = 1/|r - r'|$ is the Coulomb kernel, and the asterisk (*) denotes spatial convolution over the in-plane coordinate $\rho = (x, y)$. We solve eq 5 by expanding $\Phi_{ref}(\rho) = \sum_n \phi_n^{\text{ref}} \Phi_n(\rho)$ into an orthonormal basis of eigenfunctions specified on the domains Ω_p by $\nabla \cdot \bar{\sigma}(\rho) \nabla \Phi_n(\rho) = -q_n^2 \Phi_n(\rho)$ and subject to the “zero current” boundary conditions $\hat{n} \cdot \nabla \Phi_n$ on the domain edges $\partial \Omega_p$, with \hat{n} being the unit vector normal to the domain’s lateral boundary. These functions can be obtained with the finite element solver FEniCs⁷¹ after meshing the experimentally relevant domain.

Values for the plasmon wave vector are selected from the desired plasmon wavelength λ_p and quality factor Q according to $q_p = 2\pi(1 + iQ^{-1})/\lambda_p$.

Assembling the expansion coefficients ϕ_n^{ref} into a vector ϕ_{ref} we solve eq 5 by the matrix equation:

$$\phi_{\text{ref}} = - \left[\frac{-V \mathbf{q}_2 / (2\pi q_p)}{1 - V \mathbf{q}_2 / (2\pi q_p)} \right] \phi_{dp} \quad (6)$$

As with ϕ_{ref} , here ϕ_{dp} represents the vector of expansion coefficients for $\Phi_{dp}(\rho)$. Meanwhile, each \mathbf{q}^2 denotes a diagonal matrix of eigenvalues q_n^2 and V is the Coulomb matrix whose elements are given by $V_{m,n} = \int_{z=0} dA \Phi_m(\rho) V^* \Phi_n(\rho)$. The term in brackets in eq 6 represents the generalized reflection operator R for the system in the Φ_n basis. (The denominator is understood in the sense of a matrix inverse applied before premultiplication by the numerator.) While we

defer the derivation to forthcoming work, this reflection operator generalizes to the case of a 2D material upon a substrate with isotropic reflectivity β_{subs} as follows:

$$\mathbf{R} = \frac{\beta_{subs} - V \mathbf{q}^2 / (2\pi \kappa q_p)}{1 - V \mathbf{q}^2 / (2\pi \kappa q_p)} \quad (7)$$

Here $\kappa = (\epsilon_{subs} + 1)/2$ and $\beta_{subs} = (\epsilon_{subs} - 1)/(\epsilon_{subs} + 1)$, with ϵ_{subs} being the substrate permittivity; in this work, we take the value of 2.

We also define a symmetric matrix \mathbf{Q} in the Φ_n basis corresponding to the spatial convolution in eq 4, with elements given by $Q_{m,n} = \int_{z=0} dA \Phi_m(\rho) q \Phi_n(\rho)$. Since the Φ_n values are orthonormal, eq 4 reduces to

$$S(\rho_{dp}) \sim \frac{1}{2\pi} \phi_{dp}(\rho_{dp})^T \mathbf{Q} \mathbf{R} \phi_{dp}(\rho_{dp}) \quad (8)$$

This represents a vector norm of ϕ_{dp} with respect to the matrix \mathbf{QR} .

In summary, after computing eigenfunctions Φ_n associated with plasmonic domain geometry, we compute symmetric matrices V and \mathbf{Q} and the generalized reflectance operator \mathbf{R} . Then, in order to predict a spatial map $S(\rho_{dp})$, we simply project the incident potential emitted by our quasi-dipolar probe at each location ρ_{dp} into the Φ_n basis by evaluating the vector of coefficients $\phi_{dp,n}(\rho_{dp}) = \int dA \Phi_{dp}(\rho) \cdot \Phi_n(\rho)$ and successively applying eq 8. Although the eigenbasis Φ_n is of infinite size, projections into ϕ_{dp} decay exponentially with n when Φ_n are sorted by increasing eigenvalue q_n^2 , so a truncated basis of size $N \approx 10^3$ is in our case sufficient for a converged map of near-field scattering amplitude $|S(\rho_{dp})|$. In this way, the observables of near-field microscopy can be predicted entirely by evaluating functions in the plane of the sample ($z = 0$). This computational method may be suitable for qualitative and quantitative modeling of near-field response of other spatially inhomogeneous 2D heterostructures. Such applications and details of their unique numerical implementation will be reported elsewhere.

ASSOCIATED CONTENT

SI Supporting Information

The Supporting Information is available free of charge at <https://pubs.acs.org/doi/10.1021/acsnano.1c07011>.

Architectures and training of a convolutional neural network; data augmentation and data randomization; experimental temperature-dependent near-field images; error distribution in parameter space; and intermediate activation visualization (PDF)

AUTHOR INFORMATION

Corresponding Author

D. N. Basov — Department of Physics, Columbia University, New York, New York 10027, United States;
Email: db3056@columbia.edu

Authors

Suheng Xu — Department of Physics, Columbia University, New York, New York 10027, United States; orcid.org/0000-0002-1456-5489

Alexander. S. McLeod — Department of Physics, Columbia University, New York, New York 10027, United States
Xinzhang Chen — Department of Physics and Astronomy, Stony Brook University, Stony Brook, New York 11794, United States; orcid.org/0000-0002-6103-3848

Daniel J. Rizzo — Department of Physics, Columbia University, New York, New York 10027, United States; orcid.org/0000-0003-4587-4863

Bjarke S. Jessen — Department of Physics and Department of Mechanical Engineering, Columbia University, New York, New York 10027, United States

Ziheng Yao — Department of Physics and Astronomy, Stony Brook University, Stony Brook, New York 11794, United States

Zhicai Wang — Department of Physics and Astronomy, Stony Brook University, Stony Brook, New York 11794, United States

Zhiyuan Sun — Department of Physics, Columbia University, New York, New York 10027, United States

Sara Shabani — Department of Physics, Columbia University, New York, New York 10027, United States

Abhay N. Pasupathy — Department of Physics, Columbia University, New York, New York 10027, United States;

 orcid.org/0000-0002-2744-0634

Andrew J. Millis — Department of Physics, Columbia University, New York, New York 10027, United States; Center for Computational Quantum Physics, Flatiron Institute, New York, New York 10010, United States

Cory R. Dean — Department of Physics, Columbia University, New York, New York 10027, United States

James C. Hone — Department of Mechanical Engineering, Columbia University, New York, New York 10027, United States

Mengkun Liu — Department of Physics and Astronomy, Stony Brook University, Stony Brook, New York 11794, United States; National Synchrotron Light Source II, Brookhaven National Laboratory, Upton, New York 11973, United States

Complete contact information is available at:

<https://pubs.acs.org/10.1021/acsnano.1c07011>

Notes

The authors declare no competing financial interest.

ACKNOWLEDGMENTS

Research at Columbia on graphene/RuCl₃ interfaces was supported by the US Department of Energy (DOE), Office of Science, Basic Energy Sciences (BES), under award DE-SC0018426 (A.M., D.J.R., and D.N.B.). The development of nanofabrication and characterization techniques enabling this work was supported by the US DOE Office of Science, BES, under award DE-SC0019300 (C.R.D. and J.C.H.). The development of the universal cryogenic platform used for scanning probe measurements was supported as part of the Energy Frontier Research Center on Programmable Quantum Materials funded by the US Department of Energy (DOE), Office of Science, Basic Energy Sciences (BES), under award no. DE-SC0019443. The development of ML protocols at Columbia, Stony Brook, and Brookhaven was supported by the U.S. Department of Energy, Office of Science, National Quantum Information Science Research Centers, Co-design Center for Quantum Advantage (C2QA), under contract number DE-SC0012704. Mengkun Liu was partially supported by the RISE2 node of NASA's Solar System Exploration Research Virtual Institute under NASA Cooperative Agreement 80NSSC19MO2015. D.N.B. is Moore Investigator in Quantum Material EPIQS GBFM9455.

REFERENCES

- (1) Basov, D. N.; Fogler, M. M.; Garcia de Abajo, F. J. Polaritons in van der Waals Materials. *Science* **2016**, DOI: [10.1126/science.aag1992](https://doi.org/10.1126/science.aag1992).
- (2) Low, T.; Chaves, A.; Caldwell, J. D.; Kumar, A.; Fang, N. X.; Avouris, P.; Heinz, T. F.; Guinea, F.; Martin-Moreno, L.; Koppens, F. Polaritons in Layered Two-Dimensional Materials. *Nat. Mater.* **2017**, *16* (2), 182–194.
- (3) Basov, D. N.; Asenjo-Garcia, A.; Schuck, P. J.; Zhu, X.; Rubio, A. Polariton Panorama. *Nanophotonics* **2020**, *10* (1), 549–577.
- (4) Yao, Z.; Xu, S.; Hu, D.; Chen, X.; Dai, Q.; Liu, M. Nanoimaging and Nanospectroscopy of Polaritons with Time Resolved S-SNOM. *Adv. Opt. Mater.* **2020**, *8* (5), 1901042.
- (5) Chen, J.; et al. Optical Nano-Imaging of Gate-Tunable Graphene Plasmons. *Nature* **2012**, *487* (7405), 77–81.
- (6) Fei, Z.; Rodin, A. S.; Fogler, M. M.; McLeod, A. S.; Thiemens, M.; Lau, C. N.; Keilmann, F.; Dominguez, G.; Andreev, G. O.; Zhao, Z.; Wagner, M.; Zhang, L. M.; Neto, A. H. C.; Fei, Z.; Basov, D. N. Gate-Tuning of Graphene Plasmons Revealed by Infrared Nano-Imaging. *Nature* **2012**, *487* (7405), 82–85.
- (7) Dai, S.; Fei, Z.; Ma, Q.; Rodin, A. S.; Wagner, M.; McLeod, A. S.; Liu, M. K.; Gannett, W.; Regan, W.; Watanabe, K.; Taniguchi, T.; Thiemens, M.; Dominguez, G.; Neto, A. H. C.; Zettl, A.; Keilmann, F.; Jarillo-Herrero, P.; Fogler, M. M.; Basov, D. N. Tunable Phonon Polaritons in Atomically Thin van der Waals Crystals of Boron Nitride. *Science* **2014**, *343* (6175), 1125–1129.
- (8) Yoxall, E.; Schnell, M.; Nikitin, A. Y.; Txoperena, O.; Woessner, A.; Lundeberg, M. B.; Casanova, F.; Hueso, L. E.; Koppens, F. H. L.; Hillenbrand, R. Direct Observation of Ultraslow Hyperbolic Polariton Propagation with Negative Phase Velocity. *Nat. Photonics* **2015**, *9* (10), 674–678.
- (9) Hu, F.; Luan, Y.; Scott, M. E.; Yan, J.; Mandrus, D. G.; Xu, X.; Fei, Z. Imaging Exciton–Polariton Transport in MoSe₂ Waveguides. *Nat. Photonics* **2017**, *11* (6), 356–360.
- (10) Mrejen, M.; Yadgarov, L.; Levanon, A.; Suchowski, H. Transient Exciton-Polariton Dynamics in WSe₂ by Ultrafast Near-Field Imaging. *Sci. Adv.* **2019**, *5* (2), No. eaat9618.
- (11) Ni, G. X.; McLeod, A. S.; Sun, Z.; Wang, L.; Xiong, L.; Post, K. W.; Sunku, S. S.; Jiang, B.-Y.; Hone, J.; Dean, C. R.; Fogler, M. M.; Basov, D. N. Fundamental Limits to Graphene Plasmonics. *Nature* **2018**, *557* (7706), 530–533.
- (12) Berkowitz, M. E.; Kim, B. S. Y.; Ni, G.; McLeod, A. S.; Lo, C. F. B.; Sun, Z.; Gu, G.; Watanabe, K.; Taniguchi, T.; Millis, A. J.; Hone, J. C.; Fogler, M. M.; Averitt, R. D.; Basov, D. N. Hyperbolic Cooper-Pair Polaritons in Planar Graphene/Cuprate Plasmonic Cavities. *Nano Lett.* **2021**, *21* (1), 308–316.
- (13) Dong, Y.; Xiong, L.; Phinney, I. Y.; Sun, Z.; Jing, R.; McLeod, A. S.; Zhang, S.; Liu, S.; Ruta, F. L.; Gao, H.; Dong, Z.; Pan, R.; Edgar, J. H.; Jarillo-Herrero, P.; Levitov, L. S.; Millis, A. J.; Fogler, M. M.; Bandurin, D. A.; Basov, D. N. Fizeau Drag in Graphene Plasmonics. *Nature* **2021**, *594* (7864), 513–516.
- (14) Zhao, W.; Zhao, S.; Li, H.; Wang, S.; Wang, S.; Utama, M. I. B.; Kahn, S.; Jiang, Y.; Xiao, X.; Yoo, S.; Watanabe, K.; Taniguchi, T.; Zettl, A.; Wang, F. Efficient Fizeau Drag from Dirac Electrons in Monolayer Graphene. *Nature* **2021**, *594* (7864), 517–521.
- (15) Gerber, J. A.; Berweger, S.; O'Callahan, B. T.; Raschke, M. B. Phase-Resolved Surface Plasmon Interferometry of Graphene. *Phys. Rev. Lett.* **2014**, *113* (5), 055502.
- (16) Bylinkin, A.; Schnell, M.; Autore, M.; Calavalle, F.; Li, P.; Taboada-Gutiérrez, J.; Liu, S.; Edgar, J. H.; Casanova, F.; Hueso, L. E.; Alonso-Gonzalez, P.; Nikitin, A. Y.; Hillenbrand, R. Real-Space Observation of Vibrational Strong Coupling between Propagating Phonon Polaritons and Organic Molecules. *Nat. Photonics* **2021**, *15* (3), 197–202.
- (17) Ni, G. X.; Wang, L.; Goldflam, M. D.; Wagner, M.; Fei, Z.; McLeod, A. S.; Liu, M. K.; Keilmann, F.; Özylmaz, B.; Neto, A. H. C.; Hone, J.; Fogler, M. M.; Basov, D. N. Ultrafast Optical Switching of Infrared Plasmon Polaritons in High-Mobility Graphene. *Nat. Photonics* **2016**, *10* (4), 244–247.

- (18) Chen, X.; Hu, D.; Mescall, R.; You, G.; Basov, D. N.; Dai, Q.; Liu, M. Modern Scattering-Type Scanning Near-Field Optical Microscopy for Advanced Material Research. *Adv. Mater.* **2019**, *31* (24), 1804774.
- (19) Fei, Z.; Rodin, A. S.; Gannett, W.; Dai, S.; Regan, W.; Wagner, M.; Liu, M. K.; McLeod, A. S.; Dominguez, G.; Thiemens, M.; Neto, A. H. C.; Keilmann, F.; Zettl, A.; Hillenbrand, R.; Fogler, M. M.; Basov, D. N. Electronic and Plasmonic Phenomena at Graphene Grain Boundaries. *Nat. Nanotechnol.* **2013**, *8* (11), 821–825.
- (20) Fei, Z.; Goldflam, M. D.; Wu, J. S.; Dai, S.; Wagner, M.; McLeod, A. S.; Liu, M. K.; Post, K. W.; Zhu, S.; Janssen, G. C. A. M.; Fogler, M. M.; Basov, D. N. Edge and Surface Plasmons in Graphene Nanoribbons. *Nano Lett.* **2015**, *15* (12), 8271–8276.
- (21) Rizzo, D. J.; Jessen, B. S.; Sun, Z.; Ruta, F. L.; Zhang, J.; Yan, J.-Q.; Xian, L.; McLeod, A. S.; Berkowitz, M. E.; Watanabe, K.; Taniguchi, T.; Nagler, S. E.; Mandrus, D. G.; Rubio, A.; Fogler, M. M.; Millis, A. J.; Hone, J. C.; Dean, C. R.; Basov, D. N. Charge-Transfer Plasmon Polaritons at Graphene/ α -RuCl₃ Interfaces. *Nano Lett.* **2020**, *20* (12), 8438–8445.
- (22) Young, T.; Hazarika, D.; Poria, S.; Cambria, E. Recent Trends in Deep Learning Based Natural Language Processing. *Ieee Comput. Intell. M* **2018**, *13* (3), 55–75.
- (23) Minaee, S.; Kalchbrenner, N.; Cambria, E.; Nikzad, N.; Chenaghlu, M.; Gao, J. Deep Learning-Based Text Classification. *Acm Comput. Surv. Csur* **2021**, *54* (3), 1–40.
- (24) Stahlberg, F. Neural Machine Translation: A Review. *J. Artif. Intell. Res.* **2020**, *69*, 343–418.
- (25) Carleo, G.; Cirac, I.; Cranmer, K.; Daudet, L.; Schuld, M.; Tishby, N.; Vogt-Maranto, L.; Zdeborova, L. Machine Learning and the Physical Sciences. *Rev. Mod. Phys.* **2019**, *91* (4), 45002.
- (26) Krenn, M.; Erhard, M.; Zeilinger, A. Computer-Inspired Quantum Experiments. *Nat. Rev. Phys.* **2020**, *2* (11), 649–661.
- (27) Bedolla, E.; Padierna, L. C.; Castaneda-Priego, R. Machine Learning for Condensed Matter Physics. *J. Phys.: Condens. Matter* **2021**, *33* (5), 053001.
- (28) Kudyshev, Z. A.; Shalaev, V. M.; Boltasseva, A. Machine Learning for Integrated Quantum Photonics. *ACS Photonics* **2021**, *8*, 34.
- (29) Carrasquilla, J. Machine Learning for Quantum Matter. *Adv. Phys. X* **2020**, *5* (1), 1–37.
- (30) Carleo, G.; Troyer, M. Solving the Quantum Many-Body Problem with Artificial Neural Networks. *Science* **2017**, *355* (6325), 602–606.
- (31) Iten, R.; Metger, T.; Wilming, H.; del Rio, L.; Renner, R. Discovering Physical Concepts with Neural Networks. *Phys. Rev. Lett.* **2020**, *124* (1), 1–18.
- (32) Zhang, Y.; Mesaros, A.; Fujita, K.; Edkins, S. D.; Hamidian, M. H.; Ch'ng, K.; Eisaki, H.; Uchida, S.; Davis, J. C. S.; Khatami, E.; Kim, E. A. Machine Learning in Electronic-Quantum-Matter Imaging Experiments. *Nature* **2019**, *570* (7762), 484–490.
- (33) Chen, X.; Ren, R.; Liu, M. Validity of Machine Learning in the Quantitative Analysis of Complex Scanning Near-Field Optical Microscopy Signals Using Simulated Data. *Phys. Rev. Appl.* **2021**, *15* (1), 014001.
- (34) Chen, X.; Yao, Z.; Xu, S.; McLeod, A. S.; Corder, S. N. G.; Zhao, Y.; Tsuneto, M.; Bechtel, H. A.; Martin, M. C.; Carr, G. L.; Fogler, M. M.; Stanciu, S. G.; Basov, D. N.; Liu, M. Hybrid Machine Learning for Scanning Near-Field Optical Spectroscopy. *ACS Photonics* **2021**, *8*, 2987.
- (35) Kelley, K. P.; Ziatdinov, M.; Collins, L.; Susner, M. A.; Vasudevan, R. K.; Balke, N.; Kalinin, S. V.; Jesse, S. Fast Scanning Probe Microscopy via Machine Learning: Non-Rectangular Scans with Compressed Sensing and Gaussian Process Optimization. *Small* **2020**, *16* (37), 1–6.
- (36) Krull, A.; Hirsch, P.; Rother, C.; Schiffrian, A.; Krull, C. Artificial-Intelligence-Driven Scanning Probe Microscopy. *Commun. Phys.* **2020**, *3* (1), 1–8.
- (37) Hadji, I.; Wildes, R. P. What Do We Understand about Convolutional Networks? 2018, 1803.08834 *arXiv* (Computer Vision and Pattern Recognition) <https://arxiv.org/abs/1803.08834> (accessed March 23, 2018).
- (38) Krizhevsky, A.; Sutskever, I.; Hinton, G. E. ImageNet Classification with Deep Convolutional Neural Networks. *Commun. ACM* **2017**, *60* (6), 84–90.
- (39) Sternbach, A. J.; Hinton, J.; Slusar, T.; McLeod, A. S.; Liu, M. K.; Frenzel, A.; Wagner, M.; Iraheta, R.; Keilmann, F.; Leitenstorfer, A.; Fogler, M.; Kim, H.-T.; Averitt, R. D.; Basov, D. N. Artifact Free Time Resolved Near-Field Spectroscopy. *Opt. Express* **2017**, *25* (23), 28589.
- (40) Banerjee, A.; Bridges, C. A.; Yan, J.-Q.; Aczel, A. A.; Li, L.; Stone, M. B.; Granroth, G. E.; Lumsden, M. D.; Yiu, Y.; Knolle, J.; Bhattacharjee, S.; Kovrizhin, D. L.; Moessner, R.; Tennant, D. A.; Mandrus, D. G.; Nagler, S. E. Proximate Kitaev Quantum Spin Liquid Behaviour in a Honeycomb Magnet. *Nat. Mater.* **2016**, *15* (7), 733–740.
- (41) Gerber, E.; Yao, Y.; Arias, T. A.; Kim, E.-A. *Ab Initio* Mismatched Interface Theory of Graphene on α -RuCl₃: Doping and Magnetism. *Phys. Rev. Lett.* **2020**, *124* (10), 106804.
- (42) Taigman, Y.; Yang, M.; Ranzato, M. A.; Wolf, L. DeepFace: Closing the Gap to Human-Level Performance in Face Verification. *2014 Ieee Conf. Comput. Vis. Pattern Recognit.* **2014**, 1701–1708.
- (43) Goodfellow, I.; Bengio, Y.; Courville, A. *Deep Learning*; MIT press: Cambridge, 2016.
- (44) Chollet, F. *Deep Learning with Python*; Manning Publications: New York, 2018.
- (45) Hu, G.; Shen, J.; Qiu, C. W.; Alu, A.; Dai, S. Phonon Polaritons and Hyperbolic Response in van der Waals Materials. *Adv. Opt. Mater.* **2020**, *8* (5), 1–19.
- (46) Sternbach, A. J.; Chae, S. H.; Latini, S.; Rikhter, A. A.; Shao, Y.; Li, B.; Rhodes, D.; Kim, B.; Schuck, P. J.; Xu, X.; Zhu, X.-Y.; Averitt, R. D.; Hone, J.; Fogler, M. M.; Rubio, A.; Basov, D. N. Programmable Hyperbolic Polaritons in van der Waals Semiconductors. *Science* **2021**, *371* (6529), 617–620.
- (47) Ma, W.; Hu, G.; Hu, D.; Chen, R.; Sun, T.; Zhang, X.; Dai, Q.; Zeng, Y.; Alù, A.; Qiu, C.-W.; Li, P. Ghost Hyperbolic Surface Polaritons in Bulk Anisotropic Crystals. *Nature* **2021**, *596* (7872), 362–366.
- (48) Fei, Z.; Scott, M. E.; Gosztola, D. J.; Foley, J. J.; Yan, J.; Mandrus, D. G.; Wen, H.; Zhou, P.; Zhang, D. W.; Sun, Y.; Guest, J. R.; Gray, S. K.; Bao, W.; Wiederrecht, G. P.; Xu, X. Nano-Optical Imaging of WSe₂ Waveguide Modes Revealing Light-Exciton Interactions. *Phys. Rev. B: Condens. Matter Mater. Phys.* **2016**, *94* (8), 081402.
- (49) Hu, D.; Yang, X.; Li, C.; Liu, R.; Yao, Z.; Hu, H.; Corder, S. N. G.; Chen, J.; Sun, Z.; Liu, M.; Dai, Q. Probing Optical Anisotropy of Nanometer-Thin van der Waals Microcrystals by Near-Field Imaging. *Nat. Commun.* **2017**, *8* (1), 1471.
- (50) Atkin, J. M.; Berweger, S.; Jones, A. C.; Raschke, M. B. Nano-Optical Imaging and Spectroscopy of Order, Phases, and Domains in Complex Solids Downloaded by [University of Colorado at Boulder Libraries] at 21:13 08 December 2012. *Adv. Phys.* **2012**, *61* (6), 745–842.
- (51) Hu, D.; Chen, K.; Chen, X.; Guo, X.; Liu, M.; Dai, Q. Tunable Modal Birefringence in a Low-Loss van der Waals Waveguide. *Adv. Mater.* **2019**, *31* (27), 1807788.
- (52) Olivas, E. S.; Guerrero, J. D. M.; Martinez-Sober, M.; Magdalena-Benedito, J. R.; López, A. J. S.; Torrey, L.; Shavlik, J. *Handbook of Research on Machine Learning Applications and Trends*; IGI Global: Hershey, 2010.
- (53) Wu, Z.; Shen, C.; van den Hengel, A. Wider or Deeper: Revisiting the ResNet Model for Visual Recognition. *Pattern Recogn.* **2019**, *90*, 119–133.
- (54) Cheng, D.; Meng, G.; Cheng, G.; Pan, C. SeNet: Structured Edge Network for Sea–Land Segmentation. *Ieee Geosci. Remote S* **2017**, *14* (2), 247–251.
- (55) McLeod, A. S.; Zhang, J.; Gu, M. Q.; Jin, F.; Zhang, G.; Post, K. W.; Zhao, X. G.; Millis, A. J.; Wu, W. B.; Rondinelli, J. M.; Averitt, R.

- D.; Basov, D. N. Multi-Messenger Nanoprobes of Hidden Magnetism in a Strained Manganite. *Nat. Mater.* **2020**, *19* (4), 397–404.
- (56) Wang, L.; Xu, X. G. Scattering-Type Scanning Near-Field Optical Microscopy with Reconstruction of Vertical Interaction. *Nat. Commun.* **2015**, *6* (1), 8973.
- (57) Mooshammer, F.; Sandner, F.; Huber, M. A.; Zizlsperger, M.; Weigand, H.; Plankl, M.; Weyrich, C.; Lanius, M.; Kampmeier, J.; Mussler, G.; Grutzmacher, D.; Boland, J. L.; Cocker, T. L.; Huber, R. Nanoscale Near-Field Tomography of Surface States on (Bi 0.5 Sb 0.5) 2 Te 3. *Nano Lett.* **2018**, *18* (12), 7515–7523.
- (58) Liu, M.; Sternbach, A. J.; Basov, D. N. Nanoscale Electrodynamics of Strongly Correlated Quantum Materials. *Rep. Prog. Phys.* **2017**, *80* (1), 14501.
- (59) Qazilbash, M. M.; Brehm, M.; Chae, B.-G.; Ho, P.-C.; Andreev, G. O.; Kim, B.-J.; Yun, S. J.; Balatsky, A. V.; Maple, M. B.; Keilmann, F.; Kim, H.-T.; Basov, D. N. Mott Transition in VO₂ Revealed by Infrared Spectroscopy and Nano-Imaging. *Science* **2007**, *318* (5857), 1750–1753.
- (60) Woessner, A.; Alonso-Gonzalez, P.; Lundeberg, M. B.; Gao, Y.; Barrios-Vargas, J. E.; Navickaitė, G.; Ma, Q.; Janner, D.; Watanabe, K.; Cummings, A. W.; Taniguchi, T.; Pruneri, V.; Roche, S.; Jarillo-Herrero, P.; Hone, J.; Hillenbrand, R.; Koppens, F. H. L. Near-Field Photocurrent Nanoscopy on Bare and Encapsulated Graphene. *Nat. Commun.* **2016**, *7*, 1–7.
- (61) Sunku, S. S.; McLeod, A. S.; Stauber, T.; Yoo, H.; Halbertal, D.; Ni, G.; Sternbach, A.; Jiang, B.-Y.; Taniguchi, T.; Watanabe, K.; Kim, P.; Fogler, M. M.; Basov, D. N. Nano-Photocurrent Mapping of Local Electronic Structure in Twisted Bilayer Graphene. *Nano Lett.* **2020**, *20*, 2958.
- (62) Hoffman, J. E.; McElroy, K.; Lee, D.-H.; Lang, K. M.; Eisaki, H.; Uchida, S.; Davis, J. C. Imaging Quasiparticle Interference in Bi₂Sr₂CaCu₂O_{8+δ}. *Science* **2002**, *297* (5584), 1148–1151.
- (63) Xue, J.; Sanchez-Yamagishi, J.; Watanabe, K.; Taniguchi, T.; Jarillo-Herrero, P.; LeRoy, B. J. Long-Wavelength Local Density of States Oscillations near Graphene Step Edges. *Phys. Rev. Lett.* **2012**, *108* (1), 016801.
- (64) Wang, J.; Li, W.; Cheng, P.; Song, C.; Zhang, T.; Deng, P.; Chen, X.; Ma, X.; He, K.; Jia, J.-F.; Xue, Q.-K.; Zhu, B.-F. Power-Law Decay of Standing Waves on the Surface of Topological Insulators. *Phys. Rev. B: Condens. Matter Mater. Phys.* **2011**, *84* (23), 235447.
- (65) Hillenbrand, R.; Keilmann, F. Complex Optical Constants on a Subwavelength Scale. *Phys. Rev. Lett.* **2000**, *85* (14), 3029–3032.
- (66) Nikitin, A. Y.; Alonso-González, P.; Vélez, S.; Mastel, S.; Centeno, A.; Pesquera, A.; Zurutuza, A.; Casanova, F.; Hueso, L. E.; Koppens, F. H. L.; Hillenbrand, R. Real-Space Mapping of Tailored Sheet and Edge Plasmons in Graphene Nanoresonators. *Nat. Photonics* **2016**, *10* (4), 239–243.
- (67) Novotny, L.; Hecht, B. *Principle of Nano-Optics*; Cambridge University Press: Cambridge, 2006.
- (68) Fei, Z.; Andreev, G. O.; Bao, W.; Zhang, L. M.; McLeod, A. S.; Wang, C.; Stewart, M. K.; Zhao, Z.; Dominguez, G.; Thiemens, M.; Fogler, M. M.; Tauber, M. J.; Castro-Neto, A. H.; Lau, C. N.; Keilmann, F.; Basov, D. N. Infrared Nanoscopy of Dirac Plasmons at the Graphene–SiO₂ Interface. *Nano Lett.* **2011**, *11* (11), 4701–4705.
- (69) Aizpurua, J.; Taubner, T.; Garcia de Abajo, F. J.; Brehm, M.; Hillenbrand, R. Substrate-Enhanced Infrared Near-Field Spectroscopy. *Opt. Express* **2008**, *16* (3), 1529.
- (70) Rejaei, B.; Khavasi, A. Scattering of Surface Plasmons on Graphene by a Discontinuity in Surface Conductivity. *J. Opt.* **2015**, *17* (7), 75002.
- (71) Alnaes, M. S.; Blechta, J.; Hake, J.; Johansson, A.; Kehle, B.; Logg, A.; Richardson, C.; Ring, J.; Rognes, M. E.; Wells, G. N. The FEniCS Project Version 1.5. *Archive of Numerical Software* **2015**, DOI: 10.11588/ans.2015.100.20553.